Atmos. Meas. Tech. Discuss., 4, 4667–4715, 2011
www.atmos-meas-tech-discuss.net/4/4667/2011/
doi:10.5194/amtd-4-4667-2011

Atmospheric Measurement Techniques Discussions

Development and testing of the Active Temperature, Ozone and Moisture Microwave Spectrometer (ATOMMS) cm and mm wavelength occultation instrument

E. R. Kursinski[1], D. Ward[1], M. Stovern[1], A. C. Otarola[1,2], A. Young[1], B. Wheelwright[1], R. Stickney[1], S. Albanna[1], B. Duffy[1], C. Groppi[3], and J. Hainsworth[1]

[1]University of Arizona, Tucson, AZ 85710, USA
[2]TMT Observatory, Inc., Pasadena, CA 91109, USA
[3]Arizona State University, Tempe, AZ 85287, USA

Received: 17 March 2011 – Accepted: 2 April 2011 – Published: 22 July 2011

Correspondence to: E. R. Kursinski (kursinsk@atmo.arizona.edu)

Published by Copernicus Publications on behalf of the European Geosciences Union.

Abstract

We present initial results from testing a new remote sensing system called the Active Temperature, Ozone and Moisture Microwave Spectrometer (ATOMMS). ATOMMS is designed as a satellite to satellite occultation system for monitoring climate. We are developing the prototype instrument for an aircraft to aircraft occultation demonstration. Here we focus on field testing of the ATOMMS instrument, in particular the remote sensing of water by measuring the attenuation caused by the 22 and 183 GHz water absorption lines.

The 183 GHz line spectrum was measured along an 820 m path and compared with two spectroscopic models. This revealed that the AM 6.2 model is a much better match to the observed spectrum than the MPM93 model. These comparisons also indicate the ATOMMS amplitude errors were at the 0.3 % level. Comparisons with a hygrometer showed tracking consistent at the 0.05 mb level which is about 1 % of the absolute humidity.

Initial 22 GHz measurements along a 5.4 path between two mountaintops showed the 22 GHz channels tracking a large change in water vapor. Ground truth is much harder to establish.

1 Introduction and overview: the ATOMMS Concept

Reducing uncertainty about future climate change to support informed decision-making must be a key focus of climate research. Reducing uncertainty requires observations that determine how climate is actually changing, *independent of models*. This information is critical to assessing climate model realism. In addition, high precision, high resolution observations measuring variability are needed to tightly constrain the key processes and improve their representation in climate models in order to improve their forecasting skill.

AMTD
4, 4667–4715, 2011

The Active Temperature, Ozone and Moisture Microwave Spectrometer (ATOMMS) is a cm and mm wavelength remote sensing system we are developing to achieve unprecedented performance and attain key unfulfilled observational goals for measuring climate and reducing uncertainty about future climate.

Like GPS Radio Occultation (RO), ATOMMS is a satellite-to-satellite RO system (see Fig. 1). GPSRO is now the 4th most influential satellite system on Numerical Weather Prediction (NWP) (Cardinali, 2009) and was recommended by the Earth Decadal Survey (Anthes et al., 2007) to become a core, long-term, operational observing system. As Fig. 2 summarizes, ATOMMS extends beyond the capabilities of GPSRO by using frequencies that probe absorption lines of key atmospheric constituents (unlike GPS whose frequencies were selected specifically to minimize interactions with the atmosphere). As a result, ATOMMS has the ability to retrieve the trace gas constituents profiled by NASA's Microwave Limb Sounder (MLS) but with the much higher vertical resolution, precision, accuracy and all-weather, global sampling of GPSRO. When implemented as a constellation of small spacecraft analogous to the present COSMIC GPSRO mission, ATOMMS will yield an unprecedented combination of performance by delivering measured atmospheric profiles that are unbiased by a priori model assumptions with complete global and diurnal coverage, which are critical for monitoring and understanding climate.

ATOMMS achieves its unique performance via differential absorption by measuring signal levels at two or more frequencies simultaneously in order to reduce or eliminate many types of common mode noise. The ATOMMS prototype instrument that we are developing at the University of Arizona probes atmospheric absorption within two spectral intervals near the 22 GHz and 183 GHz absorption lines of water vapor. The low-band portion of the instrument transmits and receives 8 monochromatic tones spaced approximately every 1 GHz from 18.5 to 25.5 GHz in order to simultaneously measure and separate the absorption spectra of water vapor and liquid water (Kursinski et al., 2009). The high-band portion presently transmits and receives two tones that are tunable over the interval between 182 and 205 GHz that contains several absorption

AMTD
4, 4667–4715, 2011

lines including H_2O, O_3, N_2O and $H_2^{18}O$. We will be upgrading the high band system in the near future to measure signals at four frequencies simultaneously. The ATOMMS prototype aircraft-to-aircraft occultation demonstration is scheduled for late 2011.

Here we present some results from the ground based testing of the prototype ATOMMS instrument to date.

2 183 GHz spectra along 800 m path

In this section we discuss ATOMMS measurements taken during ground testing of the "high band" (182–205 GHz) portion of the instrument on 13 March 2010. In these tests, signals were transmitted across the University of Arizona campus over an 820 m path from the 8th floor rooftop of the Aeronautics and Mechanical Engineering building to the 11th floor rooftop of the Gould-Simpson building (see Fig. 3). We used these measurements to track changes in water vapor content along the path over the 3.5 h duration of the test.

2.1 Method

In order to recover water vapor, ATOMMS measures the attenuation of the signal due to the signal along it propagation path through the atmosphere. This is related to the atmospheric optical depth via Eq. (1). Because ATOMMS uses coherent signals, we write the absorption in terms of amplitude (rather than intensity)

$$A = A_0 e^{-\tau/2} \tag{1}$$

where A is the signal amplitude after the absorption, A_0, the amplitude of the signal in the absence of atmospheric attenuation and τ is the optical depth. The optical depth, which is proportional to the water vapor along the path, is therefore given as

$$\tau = 2\ln\left(\frac{A_0}{A}\right) \tag{2}$$

AMTD
4, 4667–4715, 2011

Thus, to determine the optical depth, we must determine A and A_0.

As noted, ATOMMS is a differential absorption system that measures signal levels at two (or more) frequencies simultaneously in order to reduce or eliminate many types of common mode noise. The relationship between the amplitudes and the optical depth difference is given in (3).

$$\tau_2 - \tau_1 = 2\ln\left(\frac{A(f_1)}{A_0(f_1)}\frac{A_0(f_2)}{A(f_2)}\right) = F(e,T,P) \quad (3)$$

where e is the water vapor partial pressure, P is the total pressure, T is atmospheric temperature, and f_1 and f_2 are frequencies near the absorption line. In the satellite geometry, $A_0(f_1)$ and $A_0(f_2)$ will be determined by measurements immediately before or after each occultation when the signal path is above the atmosphere. For rooftop measurements, determining $A_0(f_1)$ and $A_0(f_2)$ is more difficult because we cannot remove the atmosphere between the transmitter and receiver. Thus, in this early ATOMMS testing, we have been unable to calibrate our observations relative to a vacuum and retrieve the absolute amount of water vapor along the path. However, we have been able to apply a differential approach to accurately measure *changes* in water vapor with time by ratioing the amplitudes measured at each time to the amplitudes measured at some reference time.

We had planned to measure the ratio of $A_0(f_1)$ to $A_0(f_2)$ in an anechoic chamber to effectively determine the instrument response in a vacuum that would allow us to determine the absolute water vapor amount. However, our measurements taken out in the field are affected by multipath where the ATOMMS signals take not only the direct straight line signal path between the transmitter and the receiver but also at least one secondary path. The signals from the multiple paths then sum and interfere at the receiver which causes the signal amplitude to differ from that of the signal along just the direct path.

Our solution in the testing done to date is to hold the viewing geometry fixed and ratio the ATOMMS amplitude measured at each time with the ATOMMS amplitudes measured at a reference time, typically taken to be the time when the minimum water

AMTD
4, 4667–4715, 2011

vapor was measured. By holding the geometry fixed, the multipath effect remains constant and common to all measurements and therefore divides out when the amplitude ratio is formed such that the ratio yields a clean *differential* absorption spectrum. We have used this approach to achieve the results presented below.

We define the optical depth difference as

$$\Delta\tau(f, f_{\text{ref}}; e, P, T) = \tau(f; e, P, T) - \tau(f_{\text{ref}}; e, P, T) \tag{4}$$

where f is a frequency on the absorption line and f_{ref} is a frequency selected to be farther from the line center where there is relatively little absorption. For a given pressure and temperature, the optical depth difference for a given frequency and reference frequency varies approximately linearly with the integrated water vapor along the path (except for a small residual dry continuum).

$$\Delta\tau(f, f_{\text{ref}}; e, P, T) = e\, a(f; P, T) + \tau_{\text{dry}}(f; P, T) - e\, b(f_{\text{ref}}; P, T) - \tau_{\text{dry}}(f_{\text{ref}}; P, T) \tag{5}$$

The a and b terms include both the absorption line and the wet continuum. The dry continuum is small and varies slowly with frequency. Since the fractional difference between f and f_{ref} over the range of the ATOMMS "high band" frequencies is less than 10 %, the two dry continuum terms largely cancel out. So

$$\Delta\tau(f, f_{\text{ref}}; e, P, T) \cong e\,\left[a(f; P, T) - b(f_{\text{ref}}; P, T)\right] \tag{6}$$

The next step is to normalize each optical depth difference, $\Delta\tau(f, f_{\text{ref}}; e(t), P(t), T(t))$, measured at time, t, by ratioing it to the optical depth difference measured at a chosen normalization time t_0, $\Delta\tau_{\text{norm}}(f, f_{\text{ref}}; e(t_0), P(t_0), T(t_0))$ observed during the test.

$$\frac{\Delta\tau(f, f_{\text{ref}}; e(t), P(t), T(t))}{\Delta\tau(f, f_{\text{ref}}; e_{\text{norm}}(t_0), P(t_0), T(t_0))} = \frac{e(t)\,\left[a(f; P(t), T(t)) - b(f_{\text{ref}}; P(t), T(t))\right]}{e_{\text{norm}}\,\left[a(f; P(t_0), T(t_0)) - b(f_{ref}; P(t_0), T(t_0))\right]} \tag{7}$$

Therefore as long as the pressure and temperature do not vary much from t_0 to t, we can write

$$\frac{\Delta\tau(f, f_{\text{ref}}; e(t), P(t), T(t))}{\Delta\tau(f, f_{ref}; e(t_0), P(t_0), T(t_0))} \cong \frac{e(t)}{e(t_0)} \tag{8}$$

AMTD
4, 4667–4715, 2011

So the ratio of the optical depth differences at two times approximately equals the ratio of the path integrated water at those two times.

2.2 Results

For the tests performed on 13 March, our best observations were obtained when the reference frequency was set to 200.6 GHz, while the other transmit frequency was tuned over the range from 183.60 GHz to 187.50 GHz in steps of 0.15 GHz. Each individual tuned frequency was held for one second and thus it took 27 s to tune through this frequency range. This cycle of observations was repeated every 224 s during the 3.5 h duration of the test, which allowed us to make 56 estimations of the change in vapor pressure relative to a chosen normalization time, with a time spacing of 224 s.

Figure 4 shows the air pressure, temperature, and water vapor pressure measured on the day of this test by sensors on the roof of the Physics and Atmospheric Sciences (PAS) Building, which is located next door to the building where the ATOMMS receiver was operating. In the results shown below, we utilized the first set of ATOMMS measurements, centered at 16.35 h, as the normalization time. The corresponding vapor pressure from Fig. 4 is 4.15 mb. The maximum measured vapor pressure was 6.38 mb at 17.58 h, which corresponds closest in time with the 21st set of ATOMMS observations. Equation (8) is valid for all frequency pairs $(f;f_{\mathrm{ref}})$, thus we can form the ratio of the amplitude spectra at these selected times and water vapor amounts

$$\frac{A(f;f_{ref};e_{\max}(t_1),P(t_1),T(t_1))}{A(f;f_{\mathrm{ref}};e_{\mathrm{norm}}(t_0),P(t_0),T(t_0))} = A(f;e_{\max}-e_{\mathrm{norm}},P,T) \quad (9)$$

where t_1 represents the time when the maximum vapor pressure was observed.

As shown in Fig. 4, the peak to peak pressure variations during the test were about ±0.5 mb relative to a mean value of 921.4 mb for a peak to peak variation of ±0.05 %. As Fig. 5 shows, pressure variations this small will have negligible impact on the water vapor retrievals. Peak to peak temperature variations were about ±2 °C out of 293 K

AMTD
4, 4667–4715, 2011

amounting to ±0.7 %. Since the line width scales as $P/T^{0.77}$ (Payne et al., 2008), a fractional temperature error produces 0.77 times the impact of the fractional pressure error of the same magnitude. Therefore a 2 °C or 0.7 % error in temperature is equivalent to a fractional pressure error of 0.5 % or about 5 mb. According to Fig. 5, the resulting error in amplitude ratio is 0.25 % which is again very small. Therefore the resulting variations in the lineshape due to pressure and temperature essentially cancel in the ratio in Eq. (7) such that Eq. (8) and (9) are applicable to these test conditions.

Equation (9) shows that the ratio of the two spectra is another spectrum that is proportional to the water vapor difference, $e_{max} - e_{norm}$. A series of these amplitude ratio spectra can be calculated from the measured ATOMMS amplitudes. Using the corresponding measurements of pressure and temperature, a microwave propagation model can then be used to determine the value of $e_{max} - e_{norm}$ that best fits the amplitude ratio spectra obtained from ATOMMS observations of amplitude. A comparison between the ATOMMS observations and the best fit results for the AM 6.2 model (Paine et al., 2011) and the MPM 93 model (Liebe et al., 1993) is shown in Fig. 6.

Figure 6 shows that ATOMMS is useful in evaluating lineshape functions used in spectroscopic models. Specifically the Figure shows that the AM 6.2 model gives a better fit to the measured lineshape than the MPM93 model indicating that the AM 6.2 model is a significantly more accurate spectroscopic model. The $e_{max} - e_{norm}$ measured by the hygrometer on PAS was 2.23 mb. The $e_{max} - e_{norm}$ derived as the best fit of the ATOMMS measurements to the AM 6.2 model spectrum was 2.23 mb, while that derived from the best fit using the MPM93 model yielded a somewhat lower change of 2.15 mb. Since the AM 6.2 model provides a significantly better fit to the ATOMMS spectra, we use it for the rest of the results from this test.

We can apply the spectra-fitting algorithm described above at all of the 56 sets of observed ATOMMS spectra. To simplify the calculations, we used an average value for pressure of 921.4 mb and an average value for temperature of 20 °C for all of the times. As stated above the variations of pressure and temperature over the time of the ATOMMS measurements were quite small and have little effect on the best fit values

AMTD
4, 4667–4715, 2011

for water vapor changes. The results are shown in Fig. 7. The ATOMMS-derived changes in water vapor pressure track the changes measured by the PAS hygrometer including the rapid increase in water vapor near 17.4 h. It is also worth noting that the two measurement systems use entirely different physical principles to measure water vapor. The first measures changes in capacitance caused by diffusion of moisture into and out of the dielectric material in a capacitor. In contrast, ATOMMS is a mm-wavelength differential absorption spectrometer. One must also remember that an exact match is not expected because the PAS hygrometer is a point measurement while ATOMMS is measuring changes in water vapor integrated along a 820 m path.

For various reasons, including interference from nearby active cell phone towers and wireless internet, we were not able to obtain good measurements over the entire ATOMMS frequency range for this test. Still better results would be expected if we had amplitude measurements over the entire ATOMMS "high band" frequency range of 182–205 GHz. We also note that the ATOMMS measurements are inherently quite fast and ATOMMS will be able to determine water at least two orders of magnitude faster than the approximately once per 224 second sampling shown in the figures. This sampling interval was an artifact of the particular test configuration run on this day. The ATOMMS instrument will estimate water vapor at 1 s or shorter intervals.

The red curve in Fig. 5 shows the pressure sensitivity of the ATOMMS measurements via comparison with the AM model lineshape expressed as the RMS of the differences at the 27 measured ATOMMS frequencies across the range from 183.60 to 187.50 GHz. The minimum discrepancy occurs about 0.1 mb below the measured pressure. Errors of about 2 mb are distinguishable for this particular set of observations, corresponding to a fractional pressure uncertainty of about 0.2 %. Figure 5 also implies that the RMS errors in the measured ATOMMS amplitude ratios defined in Eq. (9) are about 0.3 %.

The ability to measure line shape is a key advantage of ATOMMS over GPS RO because it enables ATOMMS to determine the upper boundary of the hydrostatic integral directly from the ATOMMS observations (Kursinski et al., 2002, 2009) without relying

AMTD
4, 4667–4715, 2011

on an NWP analysis or climatology to set the upper boundary as GPS RO must do. This GPS RO sensitivity to systematic biases in those analyses limits the utility of GPS RO for climate in the mid stratosphere and above.

3 Mountaintop Observations near 22 GHz on 20 August 2010

3.1 Background

Because the 800 m distance used on campus was too short to achieve significant optical depths at 22 GHz, we designed tests to run between Mt. Bigelow (8250 ft) and Mt. Lemmon ridge (9030 ft) separated by approximately 5.4 km just north of the University of Arizona (Fig. 8a). On 20–21 August 2010 we ran our first ATOMMS mountaintop test. For cross comparisons we used three hygrometers located near the 5.4 km test path consisting of (1) the weather station in the town of Summerhaven at 7878 ft (Fig. 8), (2) the Sustainability of semi-Arid Hydrology and Riparian Areas (SAHRA) eddy correlation tower on Mt. Bigelow approximately 400 m to the east of the ATOMMS instrument on Mt. Bigelow at an elevation of 8573 ft and (3) a Buck Instruments CR4 laboratory-quality chilled mirror hygrometer located at the site of the 22 GHz transmitter on Mt. Bigelow at 8250 ft. These 3 hygrometers provide point measurements at different elevations in the vicinity of the test path. Figure 8b shows the ATOMMS 22 GHz transmitter on Mt. Lemmon looking towards the receiver located at the observatory on Mt. Bigelow.

We recorded an 11.25 h data set from 9:45 pm until 9:00 am local time during which a plume of moisture advected into the greater Tucson area increasing water vapor concentrations by a factor of two. Figure 9 shows the moisture measured by the three hygrometers with each observing an overall rise in moisture specific humidity over the test period. The Summerhaven hygrometer which is located near the point identified as “Summerhaven” in Fig. 8, begins with the largest water vapor concentration and observes the smallest change in water vapor of the three hygrometers. We suspect

AMTD
4, 4667–4715, 2011

this is associated with its location in the valley and a nocturnal thermal inversion that isolate it from larger changes in moisture at higher altitudes overnight and maintains a high moisture concentration via evapotranspiration at the surface which together hold moisture concentrations at the valley surface higher than those aloft. The two Bigelow hygrometers, track one another more closely with the SAHRA station observing the largest increase in moisture overnight. The change in specific humidity relative to the first 30 min of the test in Fig. 9b indicates that the increase in moisture was greater at higher altitudes.

3.2 22 GHz retrievals

The amplitudes of the signals measured by ATOMMS 22 GHz receiver have been reduced by absorption due to the atmospheric water vapor along the path between the two instruments according to Eq. (1). To isolate the optical depth, via Eq. (2), we must know both A and A_0. As in the campus tests, we cannot determine the A_0 term in the mountain top tests without removing the atmosphere along the 5.4 km path between the two mountains. Since calibration of the instrument in this manner is not a realistic option, we cannot determine the absolute water vapor amount but we can determine changes in water vapor using the differential approach in time.

In order to solve for the change in specific humidity, q, relative to the specific humidity start of the test, $q(t) - q(t_0)$, we must solve for differential optical depth, $\Delta\tau$, at a particular frequency, f. By taking the ratio of two received amplitudes at different times, t and t_0, we can then solve for change in optical depth.

$$\frac{A(t)}{A(t_0)}\frac{A_0(t_0)}{A_0(t)} = e^{\left(\frac{\tau(t_0)-\tau(t)}{2}\right)} \tag{10}$$

To estimate the change in optical depth, we assume that the transmitter is stable over the time period of the two observations such that the A_0 terms cancel.

$$\frac{A(t)}{A(t_0)} = e\left[\frac{-\Delta\tau}{2}\right]$$

AMTD
4, 4667–4715, 2011

$$-2\ln\left(\frac{A(t)}{A(t_0)}\right) = \Delta\tau \tag{11}$$

Converting the change in optical depth over time to a change in water vapor concentration and specific humidity requires a spectroscopic model. Using two different spectroscopic models, the AM 6.2 model and the MPM 93 model, we can estimate the optical depth knowing the pressure, temperature, and specific humidity during the time of the observations. Eq. (12) shows how differential optical depth can be related to change in specific humidity via a conversion constant, K which has units of inverse specific humidity because optical depth is unitless.

$$\Delta\tau = \tau(t) - \tau(t_0) = K\ q(t) - K\ q(t_0) = K(q(t) - q(t_0)) \tag{12}$$

By substituting differential optical depth in Eq. (11) with (12) one can solve for the change in specific humidity.

$$\Delta q = q(t) - q(t_0) = -\frac{2}{K}\ln\left(\frac{A(t)}{A(t_0)}\right) \tag{13}$$

To calculate a single conversion factor, K, over the test, we use the mean temperature, pressure and vapor pressure during the test, which are 290.92 K, 768.48 mb and 12.43 mb respectively. Using these values, we calculate the average optical depth along the observation path at 22.6 and 23.5 GHz as well as the optical depths when the water vapor mixing ratio is both increased and decreased by one g kg^{-1} relative to the mean. We then calculate the conversion factor which is the change in optical depth per change in specific humidity. The conversion factors for 22.6 and 23.5 GHz using both models are given in Table 1 below. Also shown is the fractional change in the conversion factor with respect to changes in pressure and temperature. The resulting changes in K resulting from the observed variations of 1.2 mb and 2 °C respectively in pressure and temperature are 1 % or less. Thus we can assume K is approximately constant during the data collection with minimal error.

AMTD
4, 4667–4715, 2011

3.3 22 GHz results

Figure 10 shows the change in specific humidity derived from the 22.6 (red) and 23.5 (blue) GHz channels using K derived from the AM and MPM spectroscopic models. To generate these figures, we applied the natural logarithm to the ratio of the amplitude at each time to the amplitude averaged over the first 30 min of the test to determine the changes in specific humidity relative to the average specific humidity over the first 30 min. A comparison of the results in Fig. 10a and b reveals that the 22.6 and 23.5 GHz water vapor estimates agree significantly better when the AM 6.2 model is used, again suggesting the AM model better characterizes the true 22 GHZ absorption line.

There are fine scale differences between the 22.6 and 23.5 GHz results. Some of this is likely caused by relative fluctuations in the transmit power between the channels. ATOMMS is equipped with transmitter power monitors that measure variations in transmit power. However, these were not calibrated well enough to be used to reduce differential fluctuations in the transmit power for this test. Some of the deviations between the two channels could also be due in part to non-uniform heating which can cause thermally sensitive components to heat up and cool off faster than others, resulting in differential variations not attributed to water vapor. In subsequent tests, we have taken steps to reduce temperature variations on the thermally sensitive components.

The comparison of all five estimates of the water vapor from the three hygrometers and the results derived from the 22.6 and 23.5 Hz AM 6.2 model in Fig. 11 shows overall similar behavior. The ATOMMS low band channels show a maximum overnight change in water vapor along the observation path of approximately 7 g kg^{-1}. The two hygrometers on Mt. Bigelow show changes of 5.2 to 6.3 g kg^{-1}. The differences between the ATOMMS derived water vapor and the three hygrometers appear to be dominated by spatial variations in the water vapor field itself.

It is clear from Fig. 9 that "ground truth" along the 5.4 km path between the two ATOMMS instrument above the valley at the top of the Catalina mountains is much

AMTD
4, 4667–4715, 2011

harder to establish than it was for the 800 m path length on campus. One reason is that the longer path allows for more variation along the path. Another is the steep topography which can result in much stronger diurnal variations, such as the stratification and substantial variation with height as evidenced in the three hygrometer measurements during this test. Moisture exhibits large temporal and spatial variations, causing comparisons of point and path average measurements to disagree. Much of the differences in the smaller scale variations can be attributed to the fact that the three hygrometers are point measurements whereas ATOMMS observes variations of water vapor along a path.

4 Mountaintop Measurements during a Storm on 28 August 2010

On 28 August 2010 we made a second set of measurements between Mt. Lemmon and Mt. Bigelow. During this test, a storm passed through that allowed us to measure the opacity of liquid cloud and rain droplets with ATOMMS. Figure 12 shows the temperature and dew point temperature measured by our chilled mirror hygrometer on Mt. Bigelow. We began recording ATOMMS data at noon. Water vapor varied little over the next 2.5 h until the onset of the storm. Rapid cooling (likely associated at least in part with evaporative cooling of rain) began around 14:25 h and was followed by a sharp increase in dew point around 14:45 h.

Figure 13 shows the change in opacity measured by ATOMMS at 197 GHz during the storm. These variations are due to a combination of changes in water vapor, cloud liquid water and rain. Variations associated with changes in temperature and pressure are very minor. In order to understand the cause of the changes in optical depth at 197 GHz we also examined radar and optical depths at visible wavelengths.

Because radar backscatter measurements are sensitive to the largest droplets whereas the 197 GHz measurements are sensitive to droplets of all sizes, we proceed as follows: (1) Use the radar to estimate the rain amount; (2) Estimate the 197 GHz opacity for that rain amount; (3) Subtract that opacity from the total opacity measured

AMTD
4, 4667–4715, 2011

by ATOMMS to determine the 197 GHz opacity due to clouds and (4) Convert that opacity to a cloud liquid water content (LWC). Visible wavelength opacities derived from photographs taken during the storm also provide useful independent constraints on the particle sizes.

4.1 RADAR data

The WSR-88 radar in southeastern Arizona observed the storm's evolution with 5 min resolution, 250 m range resolution and 500 m azimuthal resolution. A radar measures signals backscattered from liquid droplets much smaller than the wavelength and hence in the Rayleigh regime. The total backscatter is the sum over all backscattering particles. Treating the particle sizes as a continuous distribution yields the reflectivity, Z, which is expressed as the following integral over the particle size distribution (e.g. Fraile and Fernandez-Raga, 2009)

$$Z = \int n(D) D^6 dD \tag{14}$$

where $n(D)$ is the particle size distribution in units of m^{-4}. The reflectivity is typically given in dBz which is 10 $\log_{10}(Z/Z_0)$ where $Z_0 = 1$ $mm^6\,m^{-3}$. Figure 14 shows the time evolution of the radar backscatter along the line of sight between our ATOMMS instruments on Mt. Lemmon and Mt. Bigelow separated into 65 pixels along the path. Two elevation scans from the radar are shown at 0.88 and 1.28 degrees. While the 0.88 degree elevation scan is just above Mt. Lemmon, and therefore closer to the actual volume sampled by ATOMMS, it clearly shows more ground clutter than the 1.28 degree scan which is a bit higher above the surface. Thus the 1.28 degree scan is less noisy.

4.2 ATOMMS opacity due to liquid water

The change in opacity measured by ATOMMS at 197 GHz in Fig. 13 is due primarily to condensed liquid water because the water vapor is very close to saturation and does

AMTD
4, 4667–4715, 2011

not change much. The increase in opacity is therefore due to a combination of rain drops and cloud droplets. The cloud droplets are spherical. The rainfall rate measured during the course of this storm by two different gauges on the mountain, one at Summerhaven and one at the SAHRA flux tower was approximately 0.5 mm h^{-1}. This is comparable to the radar-derived estimates which is a light rain. Therefore we assume the rain droplets are mostly spherical which allows us to use Mie theory to understand the electromagnetic cross-sections of the droplets as a function of wavelength.

The extinction coefficient, k, at any wavelength due to spherical particles is given in Eq. (15)

$$k = \int \sigma(r) n(r) dr = \int Q(r,\lambda) \pi r^2 n(r) dr \tag{15}$$

where $Q(r,\lambda)$ is the Mie extinction efficiency which is the sum of the scattering and absorption efficiencies, $Q_{ext} = Q_{abs} + Q_{scat}$. The Mie extinction efficiency at the ATOMMS frequency of 197 GHz for cloud and rain particles is shown in Fig. 16.

The attenuation of the 197 GHz observations and the radar backscatter depend on the particle size distribution. The exponential size distribution for raindrops described by Marshall Palmer (1948) (hereafter MP) in Eq. (16) provides a simple, realistic size distribution that uses only two degrees of freedom, n_0 (m^{-3}) and α(m^{-1})

$$n(r) = n_0 \alpha e^{-\alpha r} \tag{16}$$

where r is the droplet radius. Using the MP distribution, (14) can be rewritten as

$$Z = \int n(D) D^6 dD = \int n(r) 128 r^6 dr = \int n_0 \alpha e^{-\alpha r} 128 r^6 dr = n_0 128 \int \alpha e^{-\alpha r} r^6 dr \tag{17}$$

where the upper limit is 6 mm in diameter. Equation (17) does not include the flattening effect for the larger droplets. While the present ATOMMS instrument transmits and receives circularly polarized radiation, modifying the 197 GHz receive system to measure both linear polarizations would measure the effects of the flattening.

AMTD
4, 4667–4715, 2011

4.3 Estimating rain mass and opacity from the weather radar

The standard conversion between the reflected power measured by a WSR-88D radar and rainrate is $Z = 300\,R^{1.4}$ where Z is in $\mathrm{mm}^6\,\mathrm{m}^{-3}$ and rain is in $\mathrm{mm\,h}^{-1}$ (e.g. Hunter, 1996). The corresponding derivation of rain rate (in units of $\mathrm{mm\,h}^{-1}$) from Z is therefore

$$R = \left(\frac{Z}{300}\right)^{0.71} \tag{18}$$

Rainfall is a flux of water mass equal to mass density times fall speed. The fall speed of rain drops varies with particle size (radius = r). For a simple relation between rain mass, M, and rainrate, R, we turn again to MP to get the approximate relation

$$M = 0.08R^{0.86} \tag{19}$$

where M is in $\mathrm{g\,m}^{-3}$ and R is in $\mathrm{mm\,h}^{-1}$.

The next step in understanding the opacity at 197 GHz due to rain, is to determine the dropsize distribution. With an exponential distribution of the droplet size density, the rainfall mass is given as

$$M = \int_0^\infty \rho\frac{4\pi r^3}{3}n(r)dr = \int_0^\infty \rho\frac{4\pi r^3}{3}n_0\alpha e^{-\alpha r}dr = \rho\frac{4\pi}{3}n_0\alpha\int_0^\infty r^3 e^{-\alpha r}dr = \rho\frac{24\pi}{3\alpha^3}n_0 \tag{20}$$

According to MP, the exponent in an exponential drop size distribution is related to rainfall as

$$\alpha = 4.1R^{-0.21} \tag{21}$$

where α is in mm^{-1} and R is in $\mathrm{mm\,h}^{-1}$. Combining Eqs. (20) and (21) yields a solution for n_0 in terms of M and α given in Eq. (22)

$$n_0 = \frac{3\alpha^3 M}{24\pi\rho} \tag{22}$$

AMTD
4, 4667–4715, 2011

Given n_0 and α, we combine the exponential distribution with the Mie scattering extinction efficiency shown in Fig. 15 to calculate the expected extinction coefficient and, from that, the expected extinction coefficient of the rain at the ATOMMS wavelength.

$$k_{\text{rain}} = \int \sigma(r) n_{\text{rain}}(r) dr = \int Q(r,\lambda) \pi r^2 n_0 \alpha e^{-\alpha r} dr \tag{23}$$

In applying Eq. (23) to estimate the loss of power from the radiated signal, we make the simplifying assumption of ignoring any energy forward scattered back into the beam.

The opacity measured by ATOMMS due to liquid water is the sum of the opacity due to rain and cloud

$$\tau_{197} = \int k_{197} dz = \int (k_{197\text{rain}} + k_{197\text{cloud}}) dz = \tau_{197\text{rain}} + \tau_{197\text{cloud}} \tag{24}$$

So the opacity due to cloud can be estimated as

$$\tau_{197\text{cloud}} = \tau_{197} - \tau_{197\text{rain}} \tag{25}$$

where τ_{197} is measured directly by ATOMMS and $\tau_{197\text{rain}}$ is estimated from the radar data as described above. Figure 17 shows the estimated cloud optical depth versus time, derived by subtracting the rainfall opacity estimated via Eq. (23) from the measured optical depth at 197 GHz.

4.4 Visual optical depth derived from photographs

The photographs taken from Mt. Bigelow looking toward Mt. Lemmon during the storm provide additional constraints about scattering caused by the rain and clouds at visible wavelengths that have proven useful, particularly at the onset of the storm as shown in Fig. 18. As discussed in Appendix A, in each photograph, four points were used, calibration location, near location, medium location and a far location as marked in Fig. 18. The distances to the calibration, near, medium and far location are 0.010, 0.30, 0.78 and 5.4 km respectively. In each picture, the mean red, green and blue intensities were calculated at each of the four locations.

AMTD
4, 4667–4715, 2011

At visible wavelengths, absorption by liquid water is very small and the effect of water droplets on the light is due almost entirely to scattering. Since the sky at the time was covered with clouds, the light source, S, along the path was scattered and can be approximated as homogeneous, that is, equal in all directions along the path. Under these conditions, the intensity of light measured in the photographs is given in Eq. (25) (see Appendix).

$$I = I_0 e^{-\tau_{max}} + S(1 - e^{-\tau_{max}}) \quad (26)$$

This relationship shows that the received intensity is the sum of two terms. The first term is the intensity of the light that has reflected off the object being imaged, I_0, that is then attenuated by scattering of light out of the beam path as the light propagates to the camera. The second term is the increase in intensity of light in a given pixel due to scattering into the beam path. The intensity of pure scattered light, S, is taken to be the maximum value of the pixels in a given image. Equation (25) shows that as the opacity increases, the light from the object being imaged is scattered out of the beam and replaced by light scattered into the beam from the scattered sunlight.

The simultaneous opacity measurements at ~0.5 micron and 1.5 mm wavelengths provide strong constraints on the particle sizes along the path during the onset of the storm and in particular indicate whether the drops are rain or cloud droplets. The extinction coefficient at each wavelength is given by Eq. (16). Since the signals at both wavelength bands propagate through the same atmosphere and particles, the only difference in the measured opacities is the difference in the Mie scattering efficiencies, the Q_{197} and Q_{vis} terms. As shown in Fig. 16, Q_{197} ranges from 0.015 for 5 micron radius cloud droplets to 3.5 for 0.25 mm radius rain droplets whereas Q_{vis} is approximately 2 for both cloud and rain droplet sizes. Figure 17 shows that the measured changes in opacity at 197 GHz and visible wavelengths between 14:50 h and 14:53 h were quite similar, exhibiting simultaneous rapid increases. The similar optical depths indicate that Q_{vis} and Q_{197} are comparable which can only be true if the water droplets along the path at the onset of storm were primarily rain and not cloud droplets. The agreement

AMTD
4, 4667–4715, 2011

in the timing and magnitude also provides a strong validation of the ATOMMS opacity measurements.

4.5 Derivation of cloud liquid water content

The cloud particles are sufficiently small that the attenuation at 197 GHz is due to absorption in the Rayleigh regime such that Q is proportional to x. We can therefore simplify the 197 GHz extinction coefficient due to clouds to be

$$k_{\text{cloud}} = \int_{\text{cloud}} \sigma(r) n(r) dr = \int 0.7 x \pi r^2 n(r) dr = 0.7 \frac{6\pi}{4\lambda\rho} \int \frac{4}{3} \pi r^3 n(r) \rho dr = 1.05 \frac{\pi}{\alpha\rho} \text{LWC} \quad (27)$$

where LWC is cloud liquid water content and ρ is the density of liquid water. The cloud optical depth, τ_{cloud}, measured by ATOMMS along the path between the two mountains is defined as

$$\tau_{\text{cloud}} = \int k_{\text{cloud}} dz = \overline{k}_{\text{cloud}} L = 1.05 \frac{\pi}{\alpha\rho} \overline{\text{LWC}}_{\text{cloud}} L \quad (28)$$

where $\overline{\text{LWC}}_{\text{cloud}}$ is the average liquid water content of the cloud along the path between the two ATOMMS instruments. Thus, from τ_{cloud}, we can estimate the average cloud LWC along the path as

$$\overline{\text{LWC}}_{\text{cloud}} = \frac{\tau_{\text{cloud}} \alpha\rho}{1.05\pi L} \quad (29)$$

Given that typical values of continental cloud LWC are 0.3 g m^{-3}, these estimated cloud LWC are quite reasonable (Fig. 19). The peak near 15:24 h may be associated with the cloud extending along the entire path between the two ATOMMS instruments.

Utilizing the combined radar and 197 GHz datasets is limited by several factors. First, the radar only updates every 5 min. So the radar data in Figs. 17 and 19 is only every 5 min and linearly interpolated between the points every 5 min. Second, the radar sees a larger volume than the ATOMMS beam's line of sight between the two mountains. In

AMTD
4, 4667–4715, 2011

particular, it sees the region above the ATOMMS beam. At the onset of the rain, the radar observes rain falling above the 197 GHz beam that then falls into the ATOMMS beam causing the rapid increase in opacity in the 197 GHz data around 14:52. This difference in sampling volume can cause the apparent opacity due to rain to be larger than what was measured by ATOMMS. Finally, the radar is also degraded by surface reflections (known as ground clutter) that make the radar data noisy as noted in Fig. 14.

4.6 Interpretation of what happened during the storm

4.6.1 Change in optical depths just prior to storm (14:35 h to 14:50 h)

From 14.6 h to 14.8 h, the optical depth at 197 GHz increased from 0 to 0.5. During this time interval, our chilled mirror hygrometer on Mt. Bigelow measured an increase in water vapor from 15.6 to 17.5 hPa as it rose to saturation (Fig. 12). If this same increase occurred over the entire path, the corresponding increase in optical depth at 197 GHz would have been 0.53 which is about the increase measured by ATOMMS over this period. This may not be the entire explanation because the WSR-88D RADAR also observed a small increase in reflectivity in this time interval at both the 0.88 and 1.28 degree elevation scans (Fig. 17) indicating ATOMMS should have measured some increase in opacity associated with light rain. The RADAR data is noisy particularly at the 0.88 degree elevation scan which sees a larger reflectivity and ground clutter. The 1.28 degree scan is less noisy but scans farther above the ATOMMS signal path than the 0.88 degree scan.

So the measured increase in 197 GHz opacity over this period is likely due to an increase in the water vapor concentration and may include some light rainfall. The two may in fact be related because any evaporation of rainfall would increase the vapor concentration. Had the tuning of the ATOMMS instrument operated correctly during this period, we could have separated the vapor and condensed water effects from the measurements themselves. Hopefully we will have another opportunity to do so.

AMTD
4, 4667–4715, 2011

4.6.2 Rapid increase in attenuation associated with the first rain (14:50 h to 15:00 h)

The rapid increase of approximately 1.2 in 197 GHz optical depth over the 14:50 h to 15:00 h interval is too large to be associated with water vapor given that the air is already very close to saturation. The opacity increase must therefore be due to condensed moisture in the form of clouds and rain. The storm's onset was captured at three very different wavelengths by ATOMMS, the WSR-88D radar in southeastern Arizona and in photographs. The very similar magnitude and rapid rise in the 1.5 mm and visible wavelength opacities indicates the opacity increase at the onset of the storm was caused by rain rather than via advection of clouds across the path, consistent with the simultaneous radar rain measurements.

4.6.3 Cloud with little precipitation (15:00 h to ~15:12 h)

From 15:00 h to 15:12 h, the 197 GHz opacity remained nearly constant, approximately 1.7 higher than before the storm onset while the radar reflectivity was quite small. The portion of the photographs where Mt. Lemmon had been visible became white-gray indicating visible scattering opacities greater than 2. Together, these indicate clouds are present along the path together with a little rain.

The average cloud LWC along the path during this period is about 0.15 g m^{-3}, which is about the same average rain LWC at the storm's onset at 14:55 h. The similarity of the LWC of the initial rain and subsequent cloud LWCs could just be coincidence, or it could mean that a good portion of the mass in the rain droplets was converted to cloud droplets. Certainly, as rain fell into the subsaturated clear air below cloud base, some would evaporate, cooling the air and lowering the saturation vapor pressure of the air which would then cause some of the evaporated moisture to condense into cloud droplets. This is qualitatively consistent with the rapid decrease in temperature and increase in dew point measured by the hygrometer as the storm approached.

AMTD
4, 4667–4715, 2011

4.6.4 Cloud + precipitation (~15:12 h to ~15:40 h)

By 15:20 h, Mt. Bigelow was in the clouds, experiencing light rain. The peak optical depth (relative to the pre-storm period) of 4 occurred near 15:24 h. As Fig. 19 shows, the path averaged liquid water content of the cloud at this time reached about 0.3 g m^{-3}. According to our field notes, the cloud began to clear from the Mt. Lemmon site at 15:30 h, while Mt. Bigelow remained in cloud until about 15:45 h. Given the storm's approximate direction of motion shown in Fig. 8, the decrease in cloud LWC after 15:30 h was likely associated at least in part with a decrease in the extent of the cloud along the signal path as the end of the storm passed through.

5 Summary and discussion

In summary, we have presented the first ground based test results from the ATOMMS prototype instrument. The rooftop spectra near the 183 GHz line showed that ATOMMS is a sensitive spectrometer capable of distinguishing between and evaluating two standard spectroscopic models, clearly showing the superiority of the AM 6.2 model over the MPM93 model. The results demonstrated ATOMMS' sensitivity to lineshape that will be a key to making orbiting ATOMMS observations independent of climate models, unlike GPS RO. These measurements indicate the standard deviation of the amplitude errors are ~0.3 % which is quite promising.

We showed that in these surface observations ATOMMS can measure changes in water vapor quite accurately. Our 183 GHz rooftop measurements demonstrated ATOMMS ability to measure changes in water vapor to about 0.05 mb (Fig. 7). We showed the first 22 GHz mountaintop results demonstrating the ability to probe that line to determine changes in water vapor over a 5.4 km path. Measuring changes in water vapor relative to the minimum water vapor is the same approach that will be used with the aircraft and satellite occultations. In these cases, the minimum water vapor along the path relative to which changes will be measured is a few parts per million for high

AMTD
4, 4667–4715, 2011

altitude aircraft to aircraft occultations or zero in the satellite to satellite occultations. So, in the satellite case, the changes in water vapor determined by ATOMMS will equal the absolute water vapor.

We also presented mountaintop measurements made during a storm in late August 2010. These measurements confirm that ATOMMS signals penetrate through the rain and clouds as expected. By combining ATOMMS measurements with WSR-88D data and photographs together with Mie theory, we were able to make sense of the mountaintop storm measurements and verify that the ATOMMS measurements were reasonable. Optical depths derived from photographs combined with ATOMMS measurements revealed that the storm began with rainfall rather than clouds along the ATOMMS signal path. The whiting out of the photographs caused by scattering by rain and cloud droplets reminds us of the limited utility of visible wavelengths on a planet with 60 to 70 % global cloud cover (Rossow and Shiffer, 1999). Sampling the full range of behavior of the Earth's atmosphere as required for climate and weather forecasting can only be achieved at wavelengths long enough to routinely penetrate through clouds.

The ATOMMS measurements will work well to optical depths of ∼10. Therefore the high band signals will penetrate through and measure the properties of clouds similar to those encountered here for path lengths up to about 14 km but not over much larger distances. The 22 GHz signals will propagate through much longer paths through clouds because the extinction coefficient due to liquid water is about 30 times smaller at 20 GHz than 200 GHz (Fig. 16). In fact, the liquid water opacity at 22 GHz over the 5.4 km path of this test was too small to measure reliably until we have working transmitter power monitors.

As discussed by Kursinski et al. (2009), with sampling across the line, ATOMMS measurements will provide the spectral information needed to separate the vapor from the liquid water changes. Unfortunately, during this mountaintop test, the 183 GHz band tuning measurements did not work well and we could not yet demonstrate this capability. In future tests, we demonstrate this ability to separate the vapor from the

AMTD
4, 4667–4715, 2011

liquid and better constrain the physical processes at work. For instance, it will characterize rain evaporation below cloud base via the resulting increase in water vapor content and decrease in temperature (measured via changes in linewidth), and potential subsequent condensation into clouds thereby lowering cloud base and vertically transferring energy in the atmosphere.

Another signature of rain that we will look for when the full ATOMMS instrument is running is a relative phase shift between the shorter and longer wavelength signals associated with scattering by raindrops at the shorter wavelengths (Fig. 16). The ability to do so would provide additional constraints on the raindrop size distribution.

Based on the new constraints and insight gained from these tests, we are now developing a weatherproof enclosure that will allow us to leave the ATOMMS instruments operating on the mountain for longer periods to observe weather variations and storms.

Overall, these results demonstrate some of the capabilities of ATOMMS as an open air, differential microwave spectrometer that accurately determines changes in vapor pressure, temperature and pressure and liquid water along the path between the ATOMMS transmitter and receiver.

Appendix A

Derivation of optical depths at visible wavelengths

At visible wavelengths, absorption by liquid water is very small and the effect of water droplets on the light is due almost entirely to scattering. Equation (A1) shows that the received intensity is the sum of two terms. The left hand term is the intensity of the light that has reflected off the object being imaged that is then attenuated by scattering of light out of the beam path as the light propagates to the camera. The right hand term is increase in intensity of light in that pixel due to scattering into the beam path.

$$I = I_0 e^{-\tau_{\max}} + \int_{\tau'=0}^{\tau'=\tau_{\max}} S e^{\int_{\tau"=\tau'}^{\tau"=\tau\max} - d\tau"} d\tau' \quad \text{(A1)}$$

AMTD
4, 4667–4715, 2011

where I_0 represents the intensity of the object without attenuation or brightening and S is intensity of pure scattered light and is taken to be the maximum value of the pixels in a given image. Assuming the scattered light source, S, is homogeneous, that is, equal in all directions along the path yields the relationship given in Eq. (A2).

$$I = I_0 e^{\tau \max} + S(1 - e^{-\tau_{\max}}) \tag{A2}$$

Equation (A2) shows that as the opacity increases, the light from the object being imaged is scattered out of the beam and replaced by light scattered into the beam from the cloud. Eq. (A2) can be written as

$$(I - S) = (I_0 - S)e^{-\tau_{\max}} \tag{A3}$$

Taking the ratio of Eq. (A3) for the far location from two different images yields the change in optical depth shown in Eq. (A4). This assumes that $(I_0 - S)$ doesn't change with time.

$$\ln\left(\frac{(I-S)_{\text{far}}(t_1)}{(I-S)_{\text{far}}(t_2)}\right) = \ln\left(\frac{(I_0-S)_{\text{far}}(t_1)e^{\tau_{1\text{far}}}}{(I_0-S)_{\text{far}}(t_2)e^{\tau_{2\text{far}}}}\right) = (\tau_{\text{far}}(t_2) - \tau_{\text{far}}(t_1)) \tag{A4}$$

A problem with Eq. (A4) is that the auto focus of the camera causes each picture to have somewhat different brightness and contrast. This means we can't take the direct ratio of two different images without calibrating in some sense. To get around this problem, we use the same calibration location for both pictures. By first taking the ratio of the far location to the calibration location for each picture we can eliminate camera variations as shown in Eq. (A5)

$$\ln\left(\frac{\frac{(I-S)_{\text{far}}(t_1)}{(I-S)_{\text{cal}}(t_1)}}{\frac{(I-S)_{\text{far}}(t_2)}{(I-S_{\text{cal}}(t_2))}}\right) = \ln\left(\frac{(I_0-S)_{\text{far}}(t_1)e^{-\tau_1\text{far}}}{(I_0-S)_{\text{far}}(t_2)e^{-\tau_2\text{far}}}\frac{(I_0-S)_{\text{cal}}(t_2)e^{-\tau_1\text{cal}}}{(I_0-S)_{\text{cal}}(t_1)e^{-\tau_2\text{cal}}}\right) \tag{A5}$$

After simplifying by canceling the $(I_0 - S)$ terms we get Eq. (A6), which shows we can calculate the r; celative change in visual optical depth between the far location and the

AMTD
4, 4667–4715, 2011

calibration location.

$$\ln\left(\frac{\frac{(I-S)_{\mathrm{far}}(t_1)}{(I-S)_{\mathrm{cal}}(t_1)}}{\frac{(I-S)_{\mathrm{far}}(t_2)}{(I-S)_{\mathrm{cal}}(t_2)}}\right) = (\tau_{\mathrm{far}}(t_2) - \tau_{\mathrm{far}}(t_1) + \tau_{\mathrm{cal}}(t_1) - \tau_{\mathrm{cal}}(t_2)) = \Delta\tau_{\mathrm{far}} - \Delta\tau_{\mathrm{cal}} \quad \text{(A6)}$$

The derivation works for the medium and near location simulations as well.

A1 Results

Picture 1 was used as the calibration or normalization picture to which all the following pictures visual optical depths were calculated from. In terms of Eq. (A6), the term, $\left(\frac{(I-S)\mathrm{far}(t_1)}{(I-S)_{\mathrm{cal}}(t_1)}\right)$ was calculated using Picture 1, whereas the term, $\left(\frac{(I-S)_{\mathrm{far}}(t_2)}{(I-S)_{\mathrm{cal}}(t_2)}\right)$ was calculated using the subsequent photographs so we could determine how the optical depth increased with time. Table A1 shows the relative change in optical depth for the far, medium and near locations.

Acknowledgements. This research has been funded by the National Science Foundation. We also greatfully acknowledge Greg Barron-Gafford at the Sustainability of semi-Arid Hydrological and Riperian Areas (SAHRA) and Russ Scott at the US Department of Agriculture USDA for providing us with access to data from their instruments in the several field experiments.

References

Anthes R. and Committee on Earth Science and Applications from Space: A Community Assessment and Strategy for the Future, National Research Council: Earth Science and Applications from Space: National Imperatives for the Next Decade and Beyond, Space Studies Board, The National Acamdemies Press, Washington, D.C., available at: http://www.nap.edu/catalog.php?record_id=11820, 2007.

Cardinali, C.: Forecast sensitivity to observation (FSO) as a diagnostic tool, European Center for Medium-range Weather Forecasting (ECMWF) Technical Memorandum 599, October 2009, available at: http://www.ecmwf.int/publications/, 2009.

AMTD
4, 4667–4715, 2011

Fraile, R. and M. Fernandez-Raga: On a more consistent definition of radar reflectivity, Atmósfera, 22(4), 375–385, 2009.

Hunter, S. M.: WSR-88D Radar Rainfall Estimation: Capabilities, Limitations and Potential Improvements, National Weather Digest, ISSN 0271-1052, June, 20(4), 26–38, available at: http://www.nwas.org/digest/papers/1996/Vol20No4/Pg26-Hunter.pdf, 1996.

Kursinski, E. R., Feng, D., Flittner, D., Hajj, G., Herman, B., Syndergaard, S., Ward, D., and Yunck, T.: A microwave occultation observing system optimized to characterize atmospheric water, temperature and geopotential via absorption, J. Atmos. Oceanic Technol., 19, 1897–1914, 2002.

Kursinski, E. R., Ward, D., Otarola, A., Frehlich, R., Groppi, C., Albanna, S., Schein, M., Bertiger, W., and Ross, M.: The Active Temperature Ozone and Moisture Microwave Spectrometer (ATOMMS), in: New Horizons in Occultation Research, Studies in Atmosphere and Climate, edited by: Steiner, A., Pirscher, B., Foelsche, U., and Kirchengast, G., 336 p., Hardcover, ISBN: 978-3-642-00320-2, 2009.

Liebe, H. J., Hufford, G. A., Cotton, M. G.: Propagation modeling of moist air and suspended water/ice particles at frequencies below 1000 GHz, Proc. NATO/AGARD Wave Propagation Panel, 52nd meeting, No. 3/1–10, Mallorca, Spain, 17–20 May 1993, 1993.

Marshall, J. S. and Palmer, W. M.: The distribution of raindrops with size, J. Meteor.,5, 165–166, 1948.

Paine, S.: Atmospheric Model am 6.2, available at: http://www.cfa.harvard.edu/\simspaine/am/, Harvard-Smithsonian Center for Astrophysics, Cambridge, MA, 02138, 2011.

Payne, V. H. Delamere, J. S. Cady-Pereira, K. E. Gamache, R. R. Moncet, J.-L. Mlawer, E. J. and Clough, S. A.: Air-Broadened Half-Widths of the 22- and 183-GHz Water-Vapor Lines, IEEE T. Geosci. Remote Sens., 46(11), 3601–3617, 2008.

Rossow, W. B. and Schiffer, R. A.: Advances in understanding clouds from the ISCCP, B. Am. Meteorol. Soc., 80, 2261–2287, 1999.

AMTD
4, 4667–4715, 2011

Table 1. Conversions between changes in optical depth and specific humidity.

AM6.2 Model	Avg – 1 g kg^{-1}	Avg	Avg +1 g kg^{-1}	K=[dτ] /[g kg^{-1}]	*dlnK/dP* (%/mb)	*dlnK/dT* (%/°C)
Vapor pressure (mb)	11.25	12.43	13.61			
22.6 GHz Tau [nepers]	0.359	0.394	0.428	0.0346	−0.105	−0.25
23.5 GHz Tau [nepers]	0.302	0.331	0.359	0.0285	−0.21	−0.56
MPM93 Model	**Avg – 1 g kg^{-1}**	**Avg**	**Avg +1 g kg^{-1}**	**K=[dτ] /[g kg^{-1}]**	***dlnK/dP*** **(%/mb)**	***dlnK/dT*** **(%/°C)**
Vapor pressure (mb)	11.25	12.43	13.61			
22.6 GHz Tau [nepers]	0.322	0.354	0.385	0.0312	−0.086	−0.43
23.5 GHz Tau [nepers]	0.285	0.314	0.342	0.0287	−0.049	−0.54

AMTD
4, 4667–4715, 2011

Table A1. Summary of changes in optical depth at visible wavelengths and 197 GHz.

	Far Location	Medium Location	Near Location	*S* value	197.5 GHz	197.5 GHz (10 s avg)
Picture 3 (14:52:23)	0.586	0.0407	0.013	215	0.5983	0.6355
Picture 4 (14:52:32)	0.76	0.0573	0.0362	220	0.5324	0.6463
Picture 5 (14:53:09)	1.1173	0.1139	0.0565	225	0.8698	0.822
Picture 6 (15:03:36)	2.8736	0.4451	0.2426	210	1.8558	1.8384
Picture 7 (15:10:14)	2.3435	0.9113	0.2795	205	1.9895	2.0105
Picture 8 (15:20:28)	2.7119	2.0569	1.5084	230	3.3322	3.3073

AMTD
4, 4667–4715, 2011

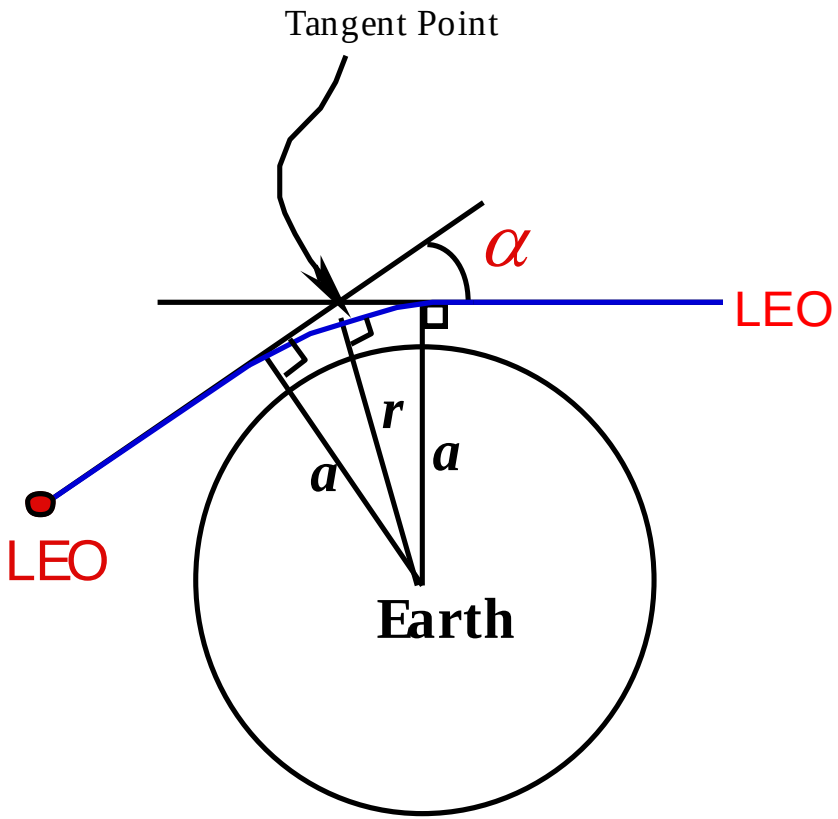

Fig. 1. ATOMMS occultation geometry.

AMTD
4, 4667–4715, 2011

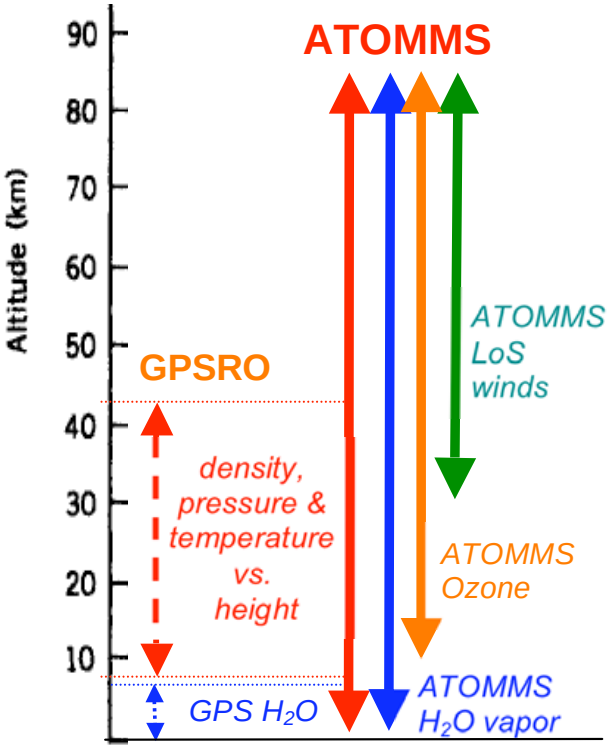

Fig. 2. Altitude comparison of ATOMMS vs. GPSRO. GPS profiles atmospheric density, pressure and temperature between the 230 K altitude in the troposphere (where water vapor begins contributing significantly to refractivity) to approximately 45 km, depending on electron densities in the ionosphere. At tropospheric temperatures warmer than 240 K, GPS refractivity primarily constrains water vapor. In contrast, ATOMMS simultaneously profiles density, pressure, temperature and water vapor from the lower troposphere to the mesopause. ATOMMS profiles ozone from the upper troposphere to the mesopause. Above the ~10 mb level, ATOMMS will also determine line of sight (LoS) winds via the Doppler shift of the center of absorption lines.

AMTD
4, 4667–4715, 2011

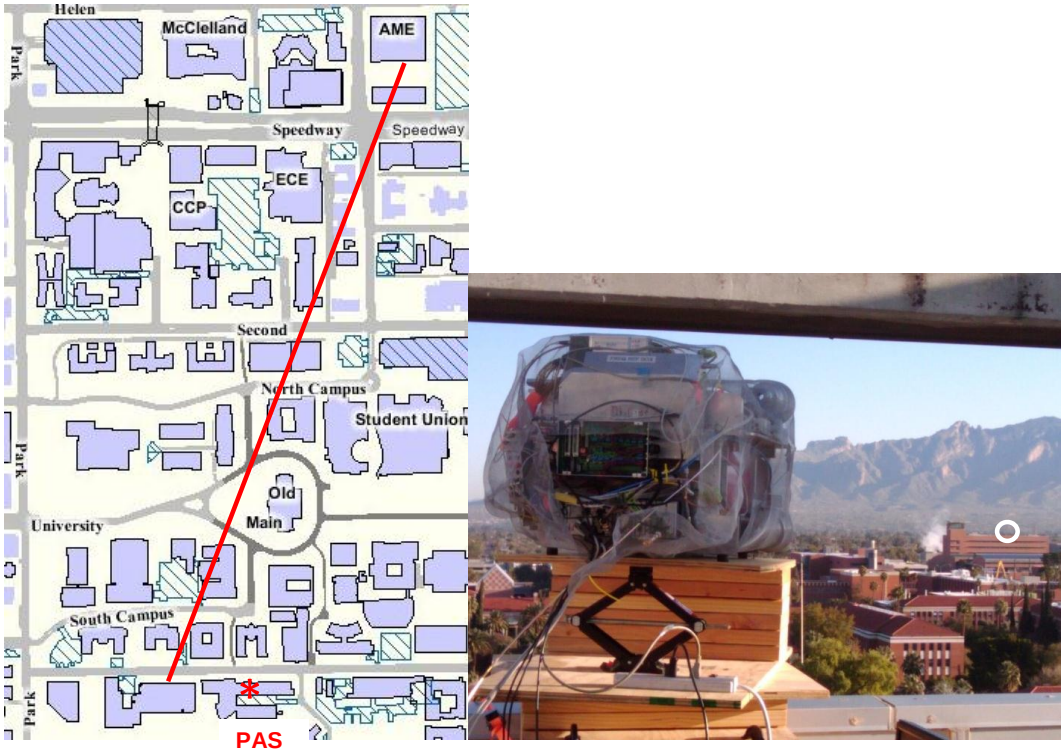

Fig. 3. Left: Map of University of Arizona showing the ATOMMS rooftop to rooftop geometry. Path length is 820 m. The red asterisk shows location of the hygrometer on the PAS building against which we compared the ATOMMS measurements. Right: ATOMMS B instrument looking toward ATOMMS A instrument on roof of AME building indicated by white circle. In the background are the Catalina Mountains where subsequent tests discussed below took place.

AMTD
4, 4667–4715, 2011

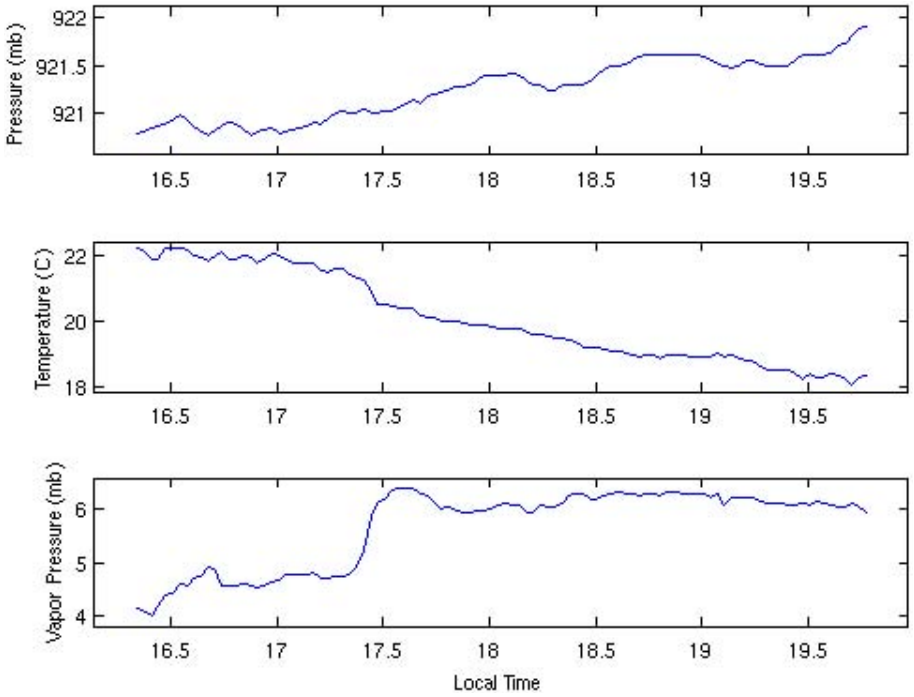

Fig. 4. The atmospheric pressure, temperature, and water vapor partial pressure measured at the PAS building during the ATOMMS rooftop tests on 13 March 2010.

AMTD
4, 4667–4715, 2011

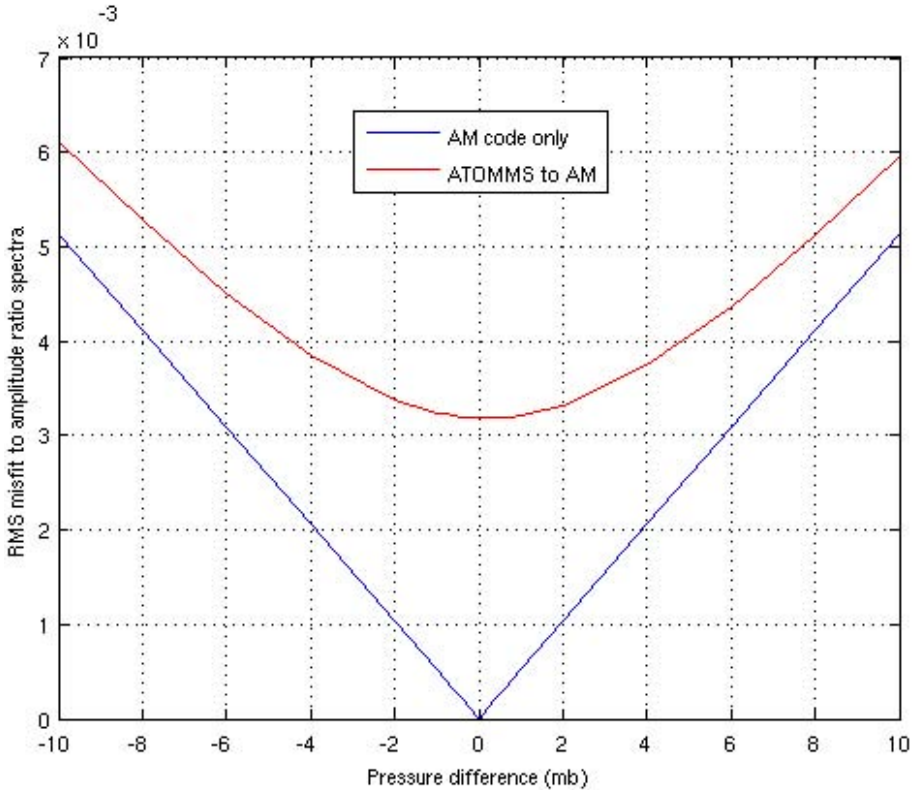

Fig. 5. Sensitivity of ATOMMS 183 GHz spectra defined in Eq. (9) to variations in pressure. The blue line is the RMS difference between the AM 6.2 model and itself as the pressure difference is varied. The red line is the difference between the ATOMMS spectra and the AM 6.2 model The best fit and minimum error occur about 0.5 mb below the measured surface pressure.

AMTD
4, 4667–4715, 2011

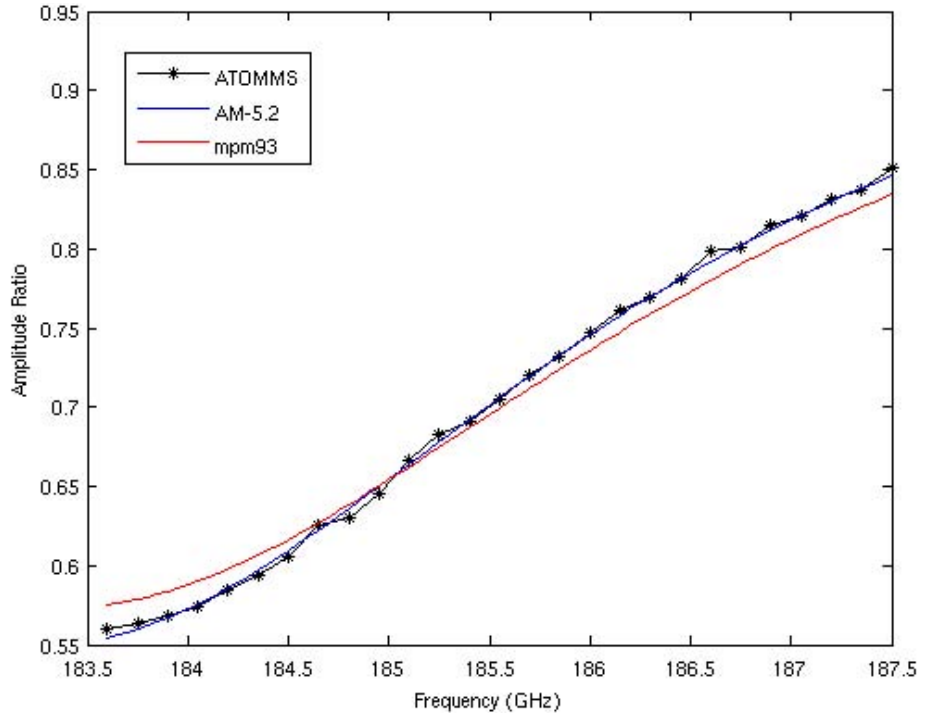

Fig. 6. Amplitude ratio as defined in Eq. (9) based on ATOMMS measurements of amplitude compared with the best fit value for e_{max}-e_{norm} to the ATOMMS amplitude ratio as computed by two microwave propagation models, AM 6.2 and MPM93.

AMTD
4, 4667–4715, 2011

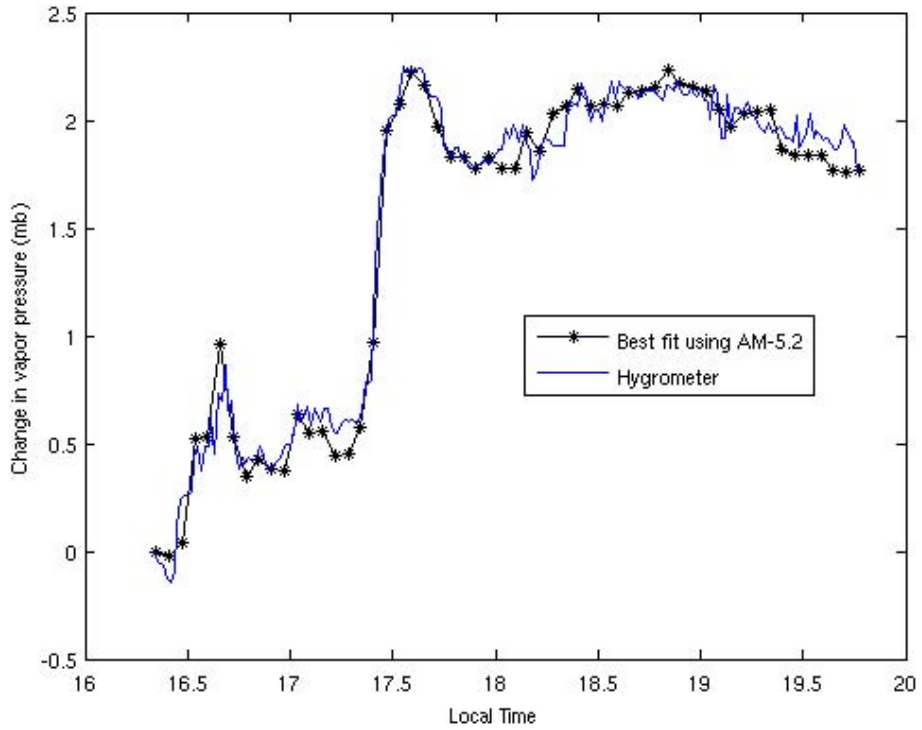

Fig. 7. Change in vapor pressure relative to first observation. The black asterisks represent the best fit changes in water vapor along the signal path to the ATOMMS amplitude ratio spectra each time an ATOMMS amplitude spectra was measured. The blue curve shows the changes in water vapor as measured by the nearby hygrometer on the PAS building.

AMTD
4, 4667–4715, 2011

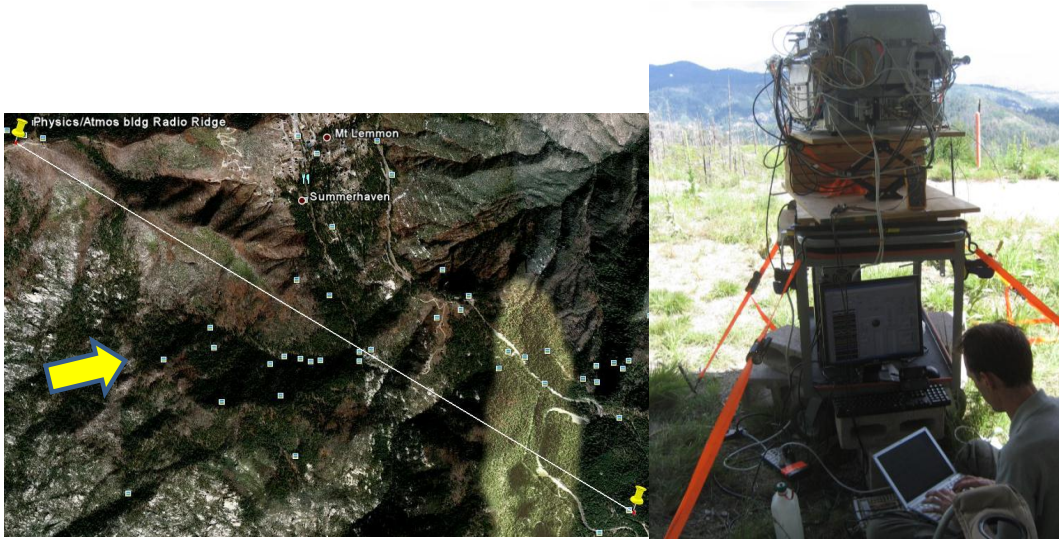

Fig. 8. Left: The Mt. Lemmon (left) to Mt. Bigelow (right) geometry. Right: Abe Young at the ATOMMS-A instrument on Mt. Lemmon. The white dome in the distance in the upper left corner of the picture is the Mt. Bigelow observatory where the ATOMMS-B instrument is located. Yellow arrow indicates the approximate direction of the propagation of the storm on 28 August 2010.

AMTD
4, 4667–4715, 2011

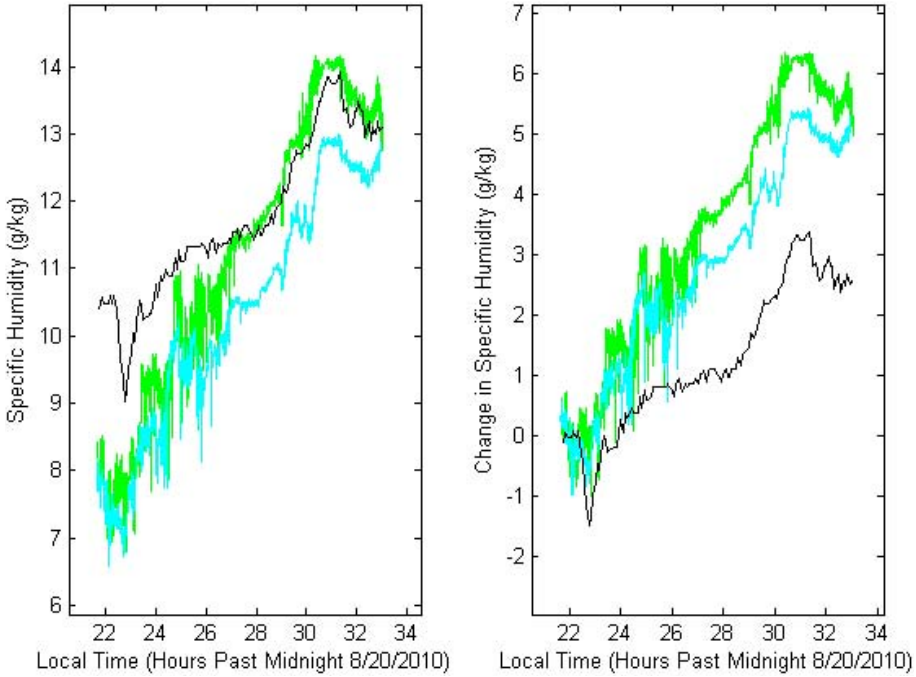

Fig. 9. Specific Humidity measurements during the test from hygrometers at Summerhaven (black), the SAHRA flux tower on Mt. Bigelow (green) and our chilled mirror hygrometer (cyan) at ATOMMS-B on Mt. Bigelow. Left: Specific humidity. Right: Change in specific humidity relative to beginning of test at 21:45 h local time.

AMTD
4, 4667–4715, 2011

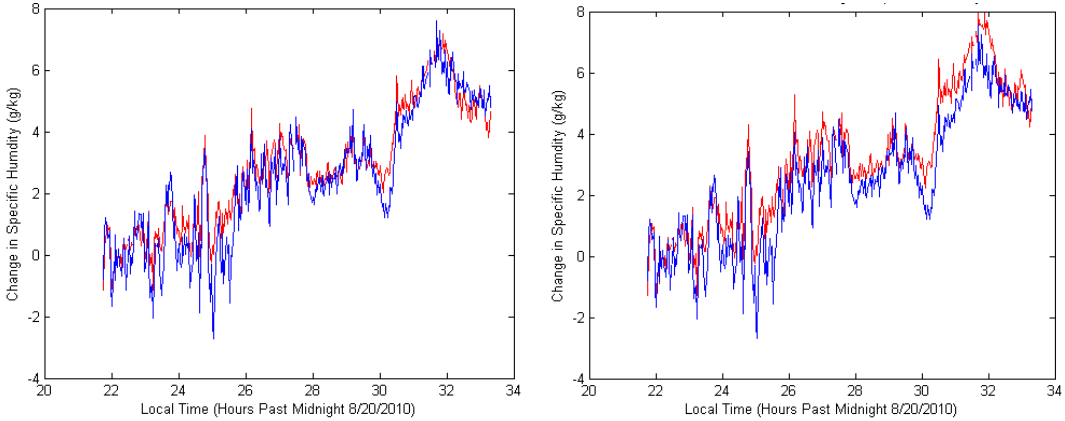

Fig. 10. Left hand panel show results of conversion to specific humidity using the AM model. Right hand figure shows conversion to specific humidity using the MPM 93 model. The 22.6 and 23.5 GHz channels are red and blue respectively.

AMTD
4, 4667–4715, 2011

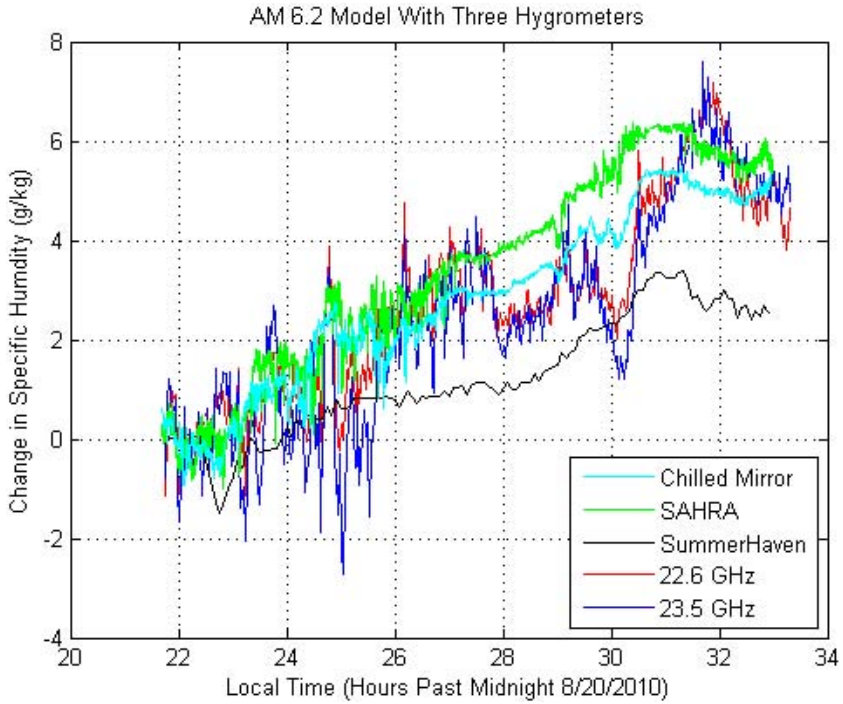

Fig. 11. Five curves each representing a particular measured change in specific humidity. The ATOMMS 22.6 and 23.5 GHz channels have been converted to specific humidity using the AM 6.2 spectroscopic model.

AMTD
4, 4667–4715, 2011

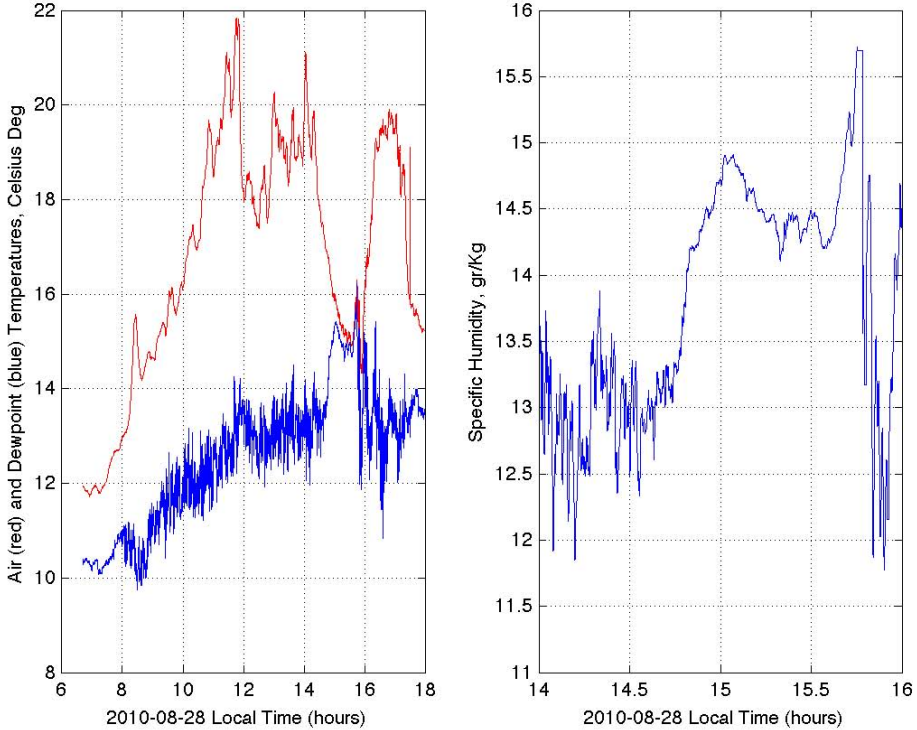

Fig. 12. Left: Measurements of the temperature and dew point from the chilled mirror hygrometer on Mt. Bigelow. Right: Specific humidity from 14:00 h to 16:00 h local time.

AMTD
4, 4667–4715, 2011

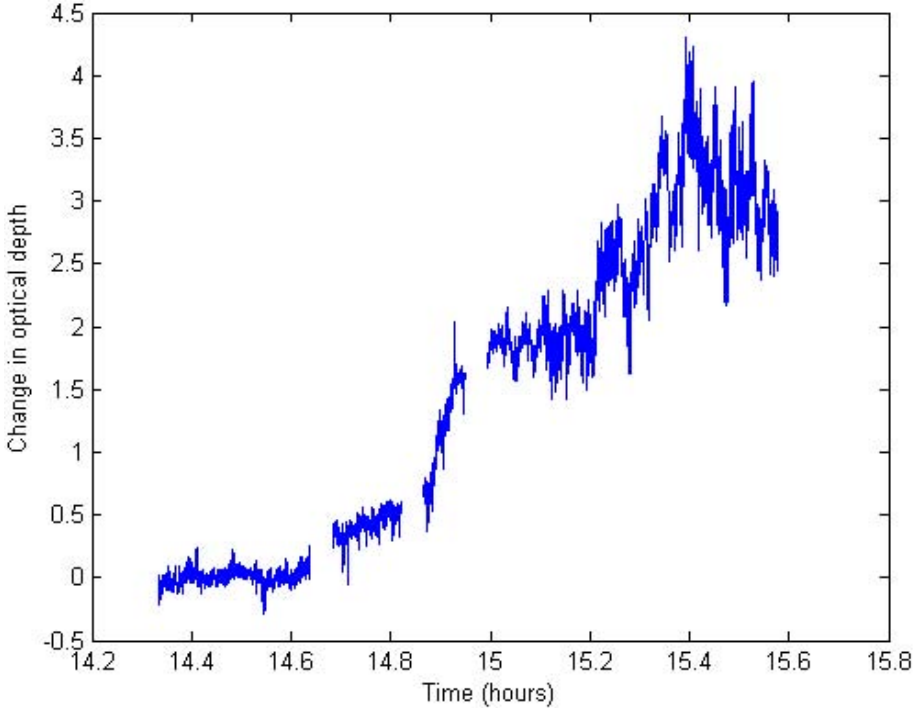

Fig. 13. Plot of change in optical depth versus time measured at 197 GHz given as $-2*\ln(A_{norm}(t))$ where the amplitude is normalized to the amplitude just before the storm hit. Outages were caused by software problems that necessitated manual restarts.

AMTD
4, 4667–4715, 2011

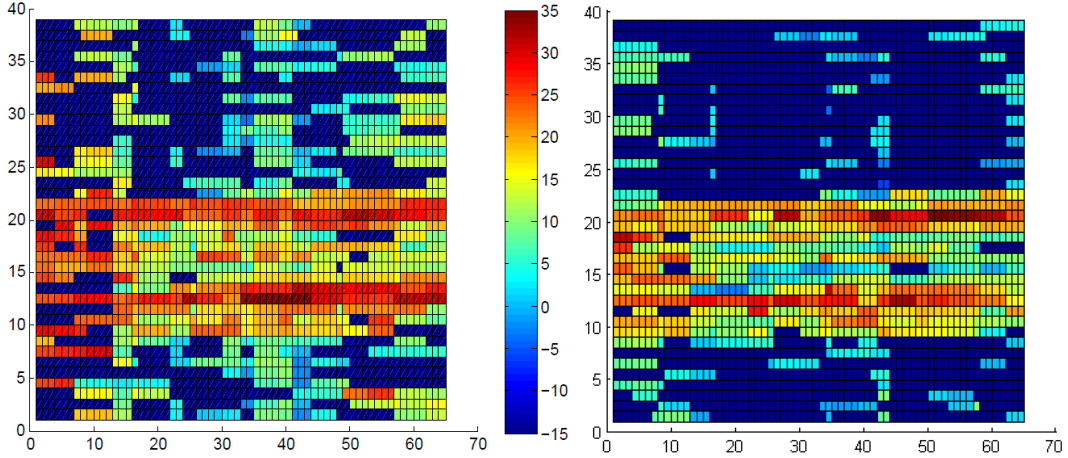

Fig. 14. Radar measured reflection in dBz, at radar elevation of **(a)** 0.88 and **(b)** 1.28 degrees, time is vertical scale in units of 5 min intervals beginning at 14:00. The left edge is Mt. Lemmon, and right hand edge is Mt. Bigelow. The 5.4 km path between them is divided into 65 equal intervals.

AMTD
4, 4667–4715, 2011

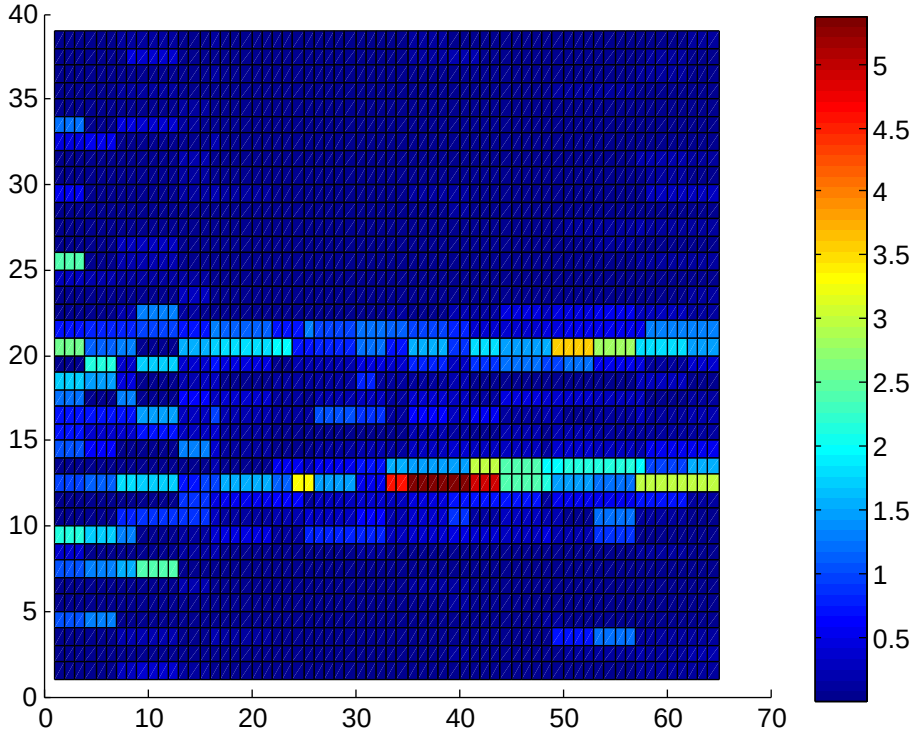

Fig. 15. Rainrate in mm h^{-1} derived from the radar data via the standard Z-R relation.

AMTD
4, 4667–4715, 2011

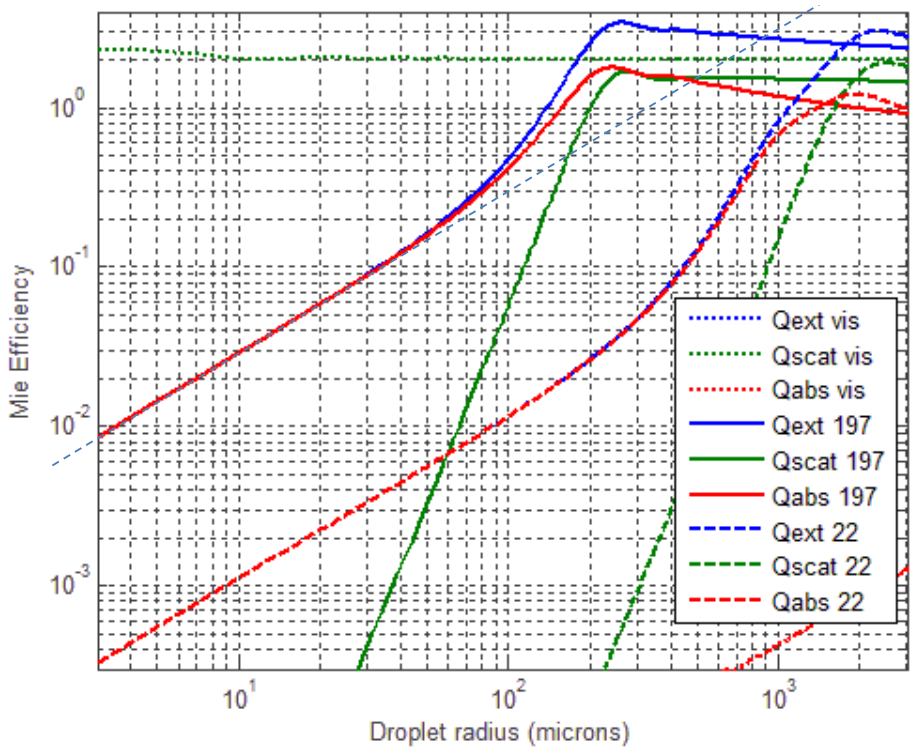

Fig. 16. Mie scattering efficiency at 22 GHz, 197 GHz and visible wavelengths versus the water droplet radius in microns. The index of refraction of the water used here is 5.5 + 2.9i, 2.83 + 1.24i and 1.3 + 1e-8 i at 22 GHz, 197 GHz and visible light respectively. The thin blue dashed line shows Rayleigh behavior at 197 GHz extrapolated to larger radii. At r=0.25 mm, the 197 GHz extinction due to Mie scattering and absorption is approximately 5 times larger than the extrapolated Rayleigh regime behavior. A typical cloud particle has a radius of 5 microns.

AMTD
4, 4667–4715, 2011

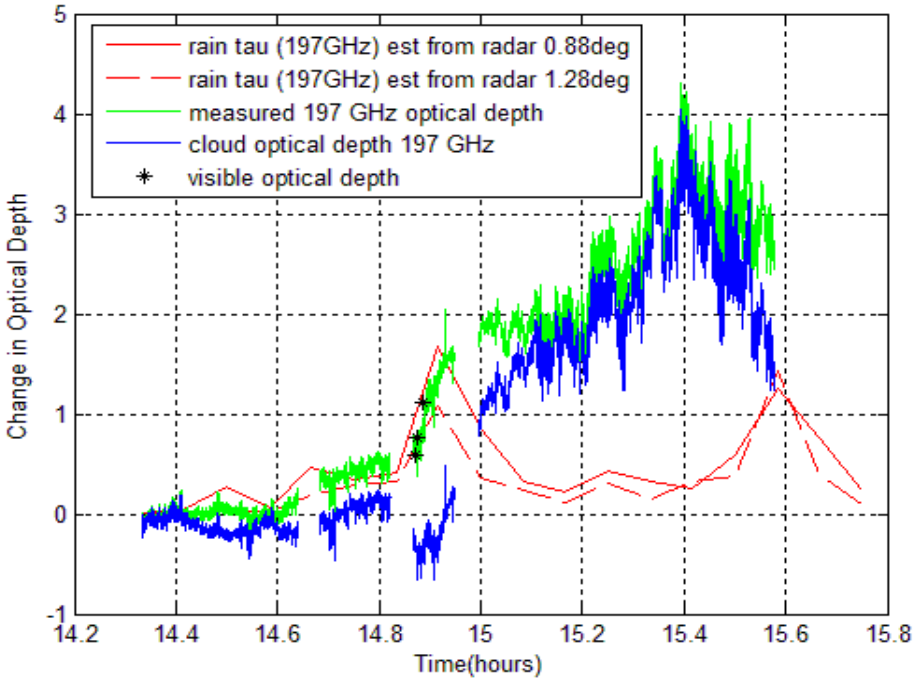

Fig. 17. Plots of the change in optical depth at 197 GHz due to rain estimated from the WSR-88 radar (red), the change in optical depth at 197 GHz based on the ATOMMS measurements (green) and the difference (blue) which is the estimated cloud amount. The asterisks are changes in optical depth at visible wavelengths derived from photographic images taken during the storm.

AMTD
4, 4667–4715, 2011

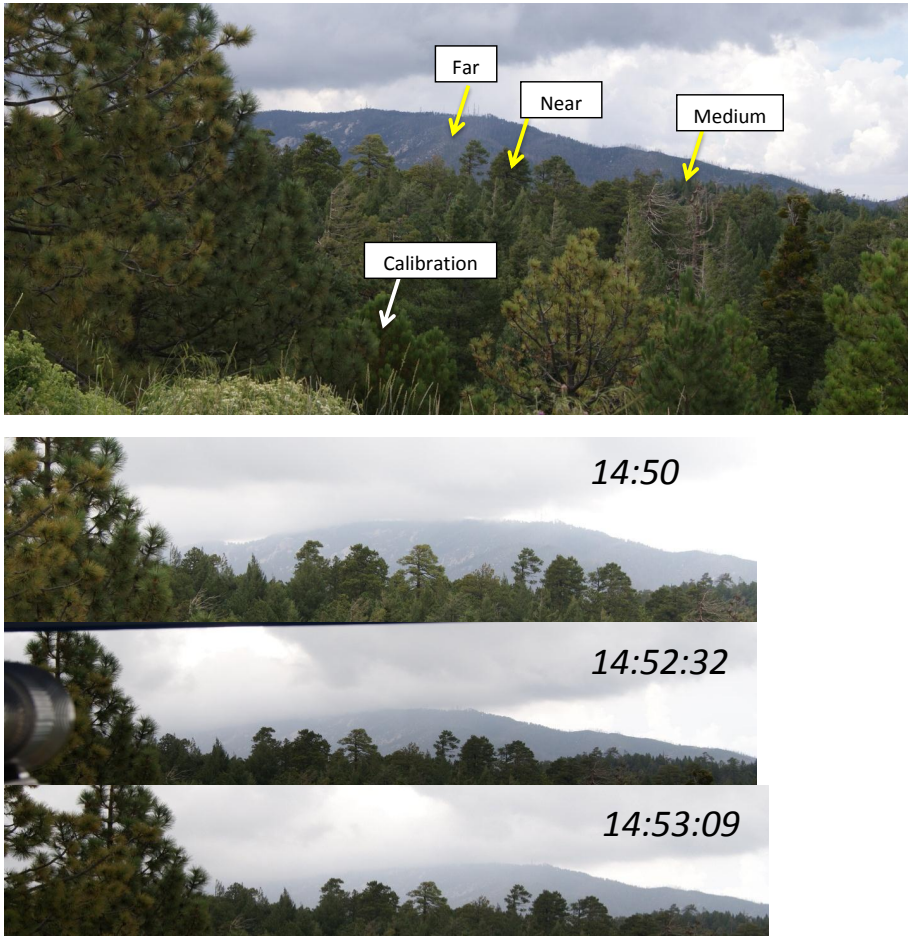

Fig. 18. View of Mt. Lemmon from Mt. Bigelow at visible wavelengths showing the evolving opacity at the onset of the storm.

AMTD
4, 4667–4715, 2011

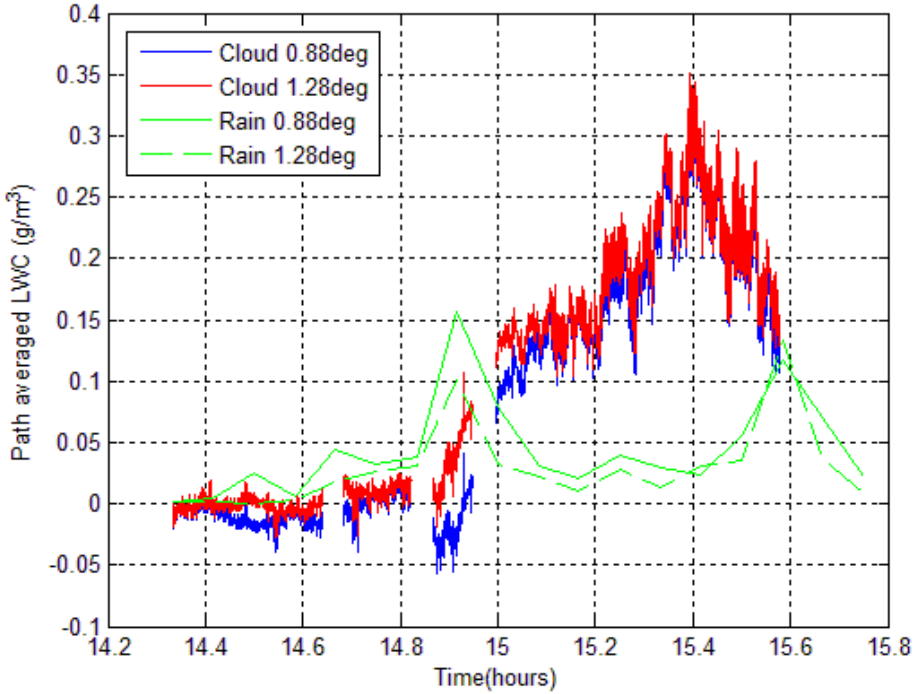

Fig. 19. Estimated average liquid water content in the rain and clouds along the 5.4 km path between the mountains.

AMTD
4, 4667–4715, 2011